Extended Scene SH Wavefront Sensor Algorithm: Minimization of Scene Content Dependent Shift Estimation Errors

Erkin Sidick
Jet Propulsion Laboratory
California Institute of Technology
4800 Oak Grove Drive
Pasadena, CA 91109
818-393-7585
Erkin.Sidick@jpl.nasa.gov

Abstract—**Adaptive Periodic-Correlation (APC) algorithm was developed for use in extended-scene Shack-Hartmann wavefront sensors. It provides high-accuracy even when the sub-images in a frame captured by a Shack-Hartmann camera are not only shifted but also distorted relative to each other. Recently we found that the shift-estimate error of the APC algorithm has a component that depends on the content of extended-scene. In this paper we assess the amount of that error and propose a method to minimize it.**

TABLE OF CONTENTS

1. INTRODUCTION

A Shack-Hartmann wavefront sensor (SH-WFS) consists of a lenslet array and a camera at the focal plane of the lenslet array; the lenslet array is placed in a plane conjugate to the plane of the wavefront error source. Its simplicity, inexpensiveness and real-time data processing capability has made the Shack-Hartmann sensor a popular wavefront sensing instrument in various areas including astronomical adaptive optics, optical testing and ocular aberrometry since its invention [1]. The conventional method used in Shack-Hartmann wavefront sensor (SH-WFS) first produces a set of spot images from a point-source, then determines the positions of the centroids of these spot images, and finally retrieves the phase information from the estimates of the offsets between these centroid positions and a set of pre-determined reference positions. When used in a closed-loop wavefront sensing and control system of a telescope, it offers high dynamic range, albeit with a lower wavefront measurement resolution than, for example, the Modified Gerchberg-Saxton (MGS) WFS approach [2]. In some applications of space-based, airborne, and ground-based adaptive optical systems, an extended-scene Shack-Hartmann sensor (ES-SHS) provides some great benefits. Poyneer found that periodic correlation method works well in this application in terms of both performance with noise and computational simplicity [3]. In that approach, the sub-pixel shift between two sub-images is determined from the location of the cross-correlation peak of the two sub-images. Recently we proposed two new approaches, the adaptive cross-correlation (ACC) algorithm [4] and adaptive periodic-correlation algorithm [5], to estimate with high accuracy the shift as large as several pixels between two extended-scene sub-images captured by a Shack-Hartmann camera (SHC). The ACC algorithm determines the positions of all of the extended-scene sub-images or cells relative to a reference cell from the linear phase of the cross-correlation spectrum of the two cells. Whereas the APC algorithm does the same from the location of cross-correlation peak of the two cells in the image-domain. We tested the shift estimation accuracy of these approaches with measured point-source and extended-scene images having several hundred cells. For point-source spot-images, we compared their phase estimation accuracies with that of a conventional centroid-finding algorithm, and obtained good agreement between the centroiding and the two new approaches. Also, we have found that the APC algorithm is more robust and more accurate than the ACC algorithm when the sub-images are not only shifted but also distorted [5].

The shift estimation accuracy of the APC algorithm depends on the content of the extended scene image captured by an SHC. In order to obtain consistent high performance from an ES-SHS under practical, varying-scene conditions, it is necessary to minimize, or ideally completely eliminate, the scene-dependent errors in sub-image shift estimate obtained with the APC algorithm. In this paper we assess the amount of the scene-dependent shift-estimate errors introduced by the APC algorithm and propose a method to minimize such errors.

2. DESCRIPTION OF THE APC ALGORITHM

The APC algorithm works in the same way as the ACC algorithm. The only difference is that, the ACC algorithm calculates the shift of a test cell relative to a reference cell from the linear phase component of the cross-correlation

978-1-4577-0557-1/12/$26.00 ©2012 IEEE

spectrum of the two cells. Whereas the APC algorithm calculates the same from the location of the cross-correlation peak in the image-domain. In our APC algorithm, the relative locations of the different SH extended-scene sub-images were determined in the following steps:

(1) Determine the center coordinates of all of the cells in Figure 1, and store these x- and y-coordinate values in a [2xM] matrix. In our case, we used the centroid locations of a point-source spot image for this purpose.

(2) Choose an N_bxN_b pixel test cell, where N_b is preferentially a power of 2 for this algorithm and the subscript "b" means "big", within each sub-image with the x- and the y-coordinates determined in Step 1 as its center, as shown with a red-box in Figure 1. In this figure, the white-frame shows an 32x32 pixel (N_b=32) cell. Also, choose one N_sxN_s small cell as a reference, where N_s<N_s and the subscript "s" means "small", preferably near the center of the extended-scene image. In Figure 2, the red-box shows an 16x16 pixel (N_s=16) small cell. In the following, we use the position variables (x, y) to denote the position dependence of a cell in the image-domain, and use (u, v) to denote the position dependence of the Fourier-transform of a cell. That is, the $r(x,y) \leftrightarrow \hat{r}(u,v)$ pair represents the reference cell in the original image and the Fourier domains, respectively. We represent the larger, N_bxN_b pixel test cells with the $S_i(x,y) \leftrightarrow \hat{S}_i(u,v)$ pair, and the smaller, N_sxN_s pixel test cells with the $s_i(x,y) \leftrightarrow \hat{s}_i(u,v)$ pair, respectively. As a standard procedure, we measure a dark image for every signal image and subtract it out from the signal image before processing the image data.

(3) Take the N_sxN_s pixel reference cell, $r(x,y)$, and calculate its Fourier-transform, $\hat{r}(u,v)$.

(4) Inside a for-loop with index i, select $S_i(x,y)$, and obtain the corresponding $\hat{S}_i(u,v)$ and $\hat{s}_i(u,v)$, respectively. Multiply $\hat{r}*(u,v)$ and $\hat{s}_i(u,v)$ to obtain a cross-correlation function in Fourier-domain, $\hat{c}_i(u,v) = \hat{r}*(u,v)\hat{s}_i(u,v)$, where "*" denotes a complex-conjugate.

(5) Inside a while-loop with index j, take the inverse-FFT (Fast Fourier-Transform) of $\hat{c}_i(u,v)$ to obtain the cross-correlation function $c_i(x,y)$ in the image-domain.

(6) Assume N_b=32, N_s=16, $[x,y]$ in $c_i(x,y)$ run from –8 to 7, and the integer-pixel peak of the $c_i(x,y)$ is located at $[X_{peak}, Y_{peak}]$. Fit a parabola to 3 data points in $c_i(x,y)$ having $y = Y_{peak}$ and $x = X_{peak}$-1, X_{peak}, X_{peak}+1, respectively, and determine the real-number pixel location of the $c_i(x,y)$ peak in the horizontal or the x-direction, δx_{ij}. Do the same in the vertical or y-direction by fitting a parabola to 3 data points of the $c_i(x,y)$ having $X = X_{peak}$ and $y = Y_{peak}$-1, Y_{peak}, Y_{peak}+1, respectively,, and obtain δy_{ij}. In practice, each peak-location-finding is done analytically using 3 data points to determine 3 unknowns, a, b, and x_{max}[3]:

$$y = a(x - x_{max})^2 + b \tag{1}$$

The [δx_{ij}, δy_{ij}] pair represent the incremental shifts in the x- and y-directions, respectively. Also accumulate these incremental shifts to obtain the total shifts [Δx_{ij}, Δy_{ij}] up to the current peak-finding iterations:

$$\Delta x_{ij} = \sum_j \delta x_{ij}, \qquad \Delta y_{ij} = \sum_j \delta y_{ij} \tag{2}$$

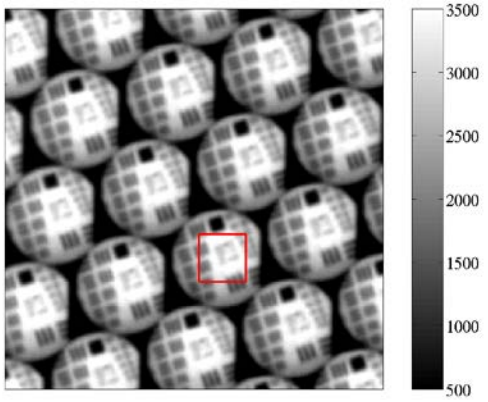

Figure 1 – A measured SHS extended-scene sub-image array. The red-colored box shows a 32x32 pixel (N_b=32) big cell.

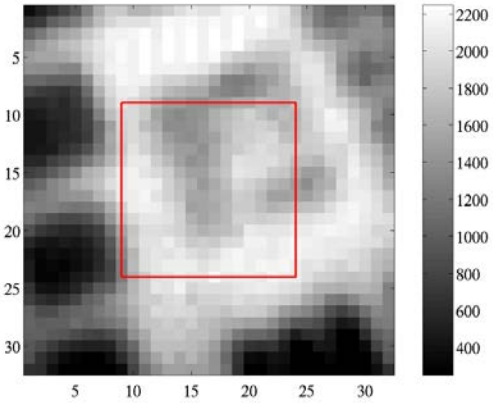

Figure 2 –One 32x32 pixel big cell of the sub-image array shown in Figure 1. The red-colored box shows a 16x16 pixel (N_s=16) small cell.

(7) Obtain a new $S_{ij}(x,y)$, a new version of $S_i(x,y)$ shifted to match with the $r(x,y)$, from the inverse-FFT of $\hat{S}_{ij}(u,v) = \hat{S}_i(u,v)\exp[-j2\pi(\Delta x_{ij}u + \Delta y_{ij}v)]$. Repeat the while-loop (Steps 5-6) until the radial incremental shift $\delta r_{ij} = \sqrt{\delta x_{ij}^2 + \delta y_{ij}^2}$ becomes less than a pre-

determined tolerance value, such as 0.01 pixel, or until the total number of iterations, such as 15, is reached.

(8) Repeat the for-loop (Steps 4 through 7) for all test cells $S_i(x,y)$.

It should be pointed out that $\hat{r}(u,v)$ needs to be calculated only once for each SHC image, and $\hat{S}_i(u,v)$ needs to be calculated only once for each test cell. If the shift estimate for a particular test cell $s_i(x,y)$ is completed in 4 shift-finding iterations, for example, then one needs to carry out inverse-FFT on $\hat{c}_{ij}(u,v)$ for 4 times (Steps 4-7), and calculate the inverse-FFT of $\hat{S}_{ij}(u,v) = \hat{S}_i(u,v)\exp[-j2\pi(\Delta x_{ij}u + \Delta y_{ij}v)]$ also 4 times.

3. SHIFT ESTIMATE ACCURACY

The process of sub-image shift estimation described in the previous section yields a grid of sub-image in an SHC image. To determine the wavefront error at the lenslet plane, we need two sets of sub-image locations. One (or the set of reference locations) corresponds to a reference image, and the other (or the set of test locations) corresponds to a test image. By subtracting the reference locations from the test ones, we obtain a 2-dimensional image-shift map specified by two shift vectors $[\Delta\vec{x}, \Delta\vec{y}]$. Each element of this map corresponds to the local tilt of the wavefront at the corresponding lenslet location. Depending on how the reference locations are determined in ES-SHS, the shift estimate process can be divided into two categories: Differential-mode and absolute-mode. In the following, we briefly describe those two modes and the corresponding shift estimate accuracy.

Differential-Mode

In this mode, both the reference and the test locations are determined using the same scene, such as the one shown in Figure 1. This is usually the case in an optical system laboratory. We have evaluated the differential-mode shift estimate accuracy of the APC algorithm using some image data obtained on the Advanced Wavefront-sensing and Control Testbed (AWCT) at Jet Propulsion Laboratory (JPL), California Institute of Technology [6]. The testbed was described in details in Ref. [6], so its description will not be repeated here. The sub-images produced by this testbed have a size of about 35x35 pixels. Several different scenes were implemented on that testbed, but the results obtained from only one scene, the one shown in Figure 1, are presented here.

Figure 3 shows an example of the SH wavefront sensing conducted on our AWCT testbed. It is an Optical Path-Difference (OPD) map and was obtained by analyzing two frames of extended-scene images with the APC algorithm. The extended-scene is the same as in Figure 1. The ES-SHS system includes a deformable-mirror (DM) installed to a plane conjugate to the exit pupil of the system. The reference image was taken with a set of actuator commands corresponding to a "flat-state", a state where the wavefront error of the system is minimized, and the test image was taken after applying different amounts of voltages to four actuators in addition to their "flat-state" voltages. Figure 4 is an image-shift diagram resulted in the OPD map in Figure 3. If we separate the areas of four poked actuators on Figure 4, and the plot the radial shifts falling inside those four areas, we obtain an image shift distribution plot, Figure 5. This plot shows that the largest radial shift in Figure 4 obtained with the APC algorithm is less than 0.02 pixels. This result proves that the APC algorithm is highly accurate in the differential-mode. This is one of the most significant findings of this study.

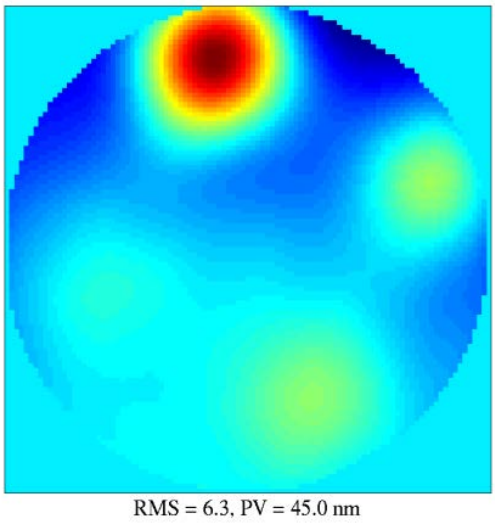

Figure 3 –Optical Path-Difference (OPD) map obtained in a differential-mode ES-SHS experiment.

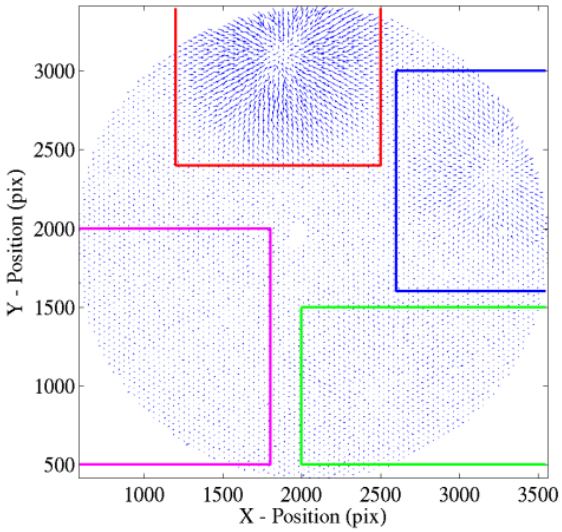

Figure 4 –Image shift diagram resulted in the OPD map shown in Figure 3.

Absolute-Mode

In this mode, different scenes are used for the reference and the test images. This is the typical case of the real operation of an ES-SHS, such as in a telescope used for remote-sensing of a planet's surface from space. In such an application, the scene to be captured as the test images changes constantly, and the reference image locations needs to be determined in advance. No adequate experimental SHC image data have been available for us so far to evaluate the accuracy of the APC algorithm in the absolute-mode. Even though some SHC images have been taken on our AWCT testbed with different scenes, they were done so by moving some hardware, namely, a filter-wheel, in the optical system. As a result, such images could not be used for determining the accuracy of the APC algorithm in absolute-mode. Therefore, in the following section, we evaluate the absolute-mode shift estimate accuracy of the APC algorithm by using half-measured, half-synthesized extended scene images. Using such images, we also determine the scene-dependent shift estimate errors and propose a method to minimize them.

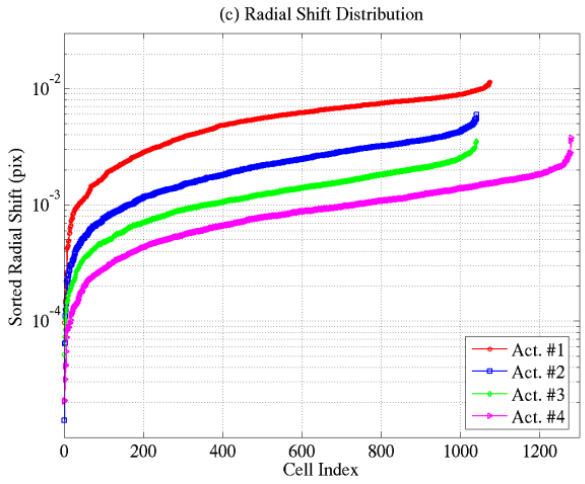

Figure 5 –Distribution of radial image shifts inside the four areas in Figure 4.

4. Scene Dependent Shift Estimate Error and Its Minimization

The extended scene we used to study the absolute-mode shift estimate error is a 512x512 pixel satellite photo shown in Figure 6. It is the same photo we used to study the dependence of our Adaptive Cross-Correlation algorithm performance on the extended scene image quality [7]. A 65x65 pixels square-shaped sub-image is indicated with a yellow-box on this figure, and is shown in Figure 7 after multiplied with a circular mask. Figure 8 shows the part of a point-source spot-image taken on another ES-SHS testbed

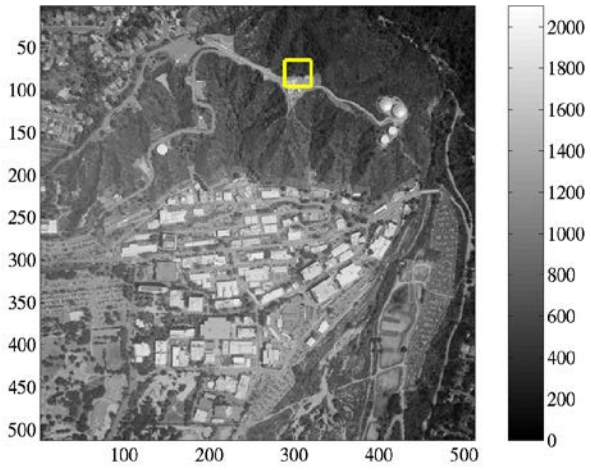

Figure 6 –A 512x512 pixels satellite photo. The yellow-box shows a 65x65 pixels sub-image.

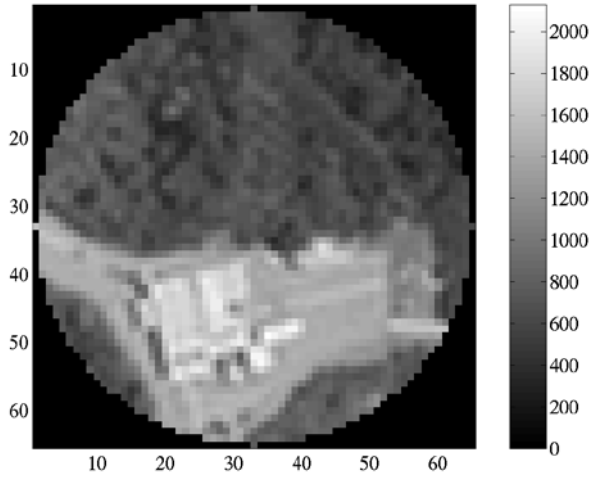

Figure 7 –A 65x65 pixels sub-image corresponding to the yellow-box on Figure 6.

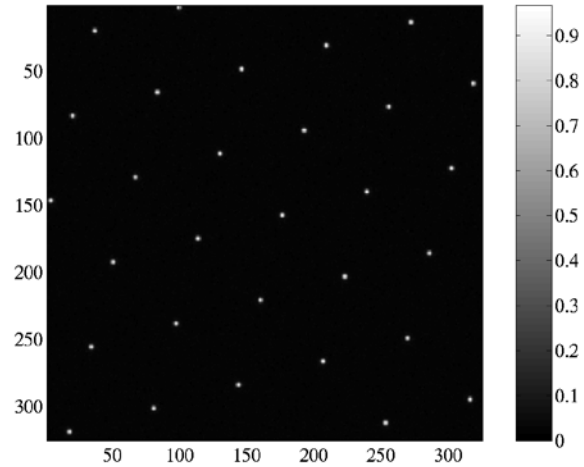

Figure 8 –Part of a measured point-source spot-image.

at JPL [8]. The sub-image size is about 65x65 pixels and the whole image has a total of 510 sub-images. The original image was taken with a 12-bit camera and has a gray-scale of 0 – 4095. We chose from the image in Figure 7 a total of 180 sub-images similar to the one shown in Figure 8 such that they are interleaved by 64 pixels in both the x- and the y-directions. Then we convolved those 180 sub-images

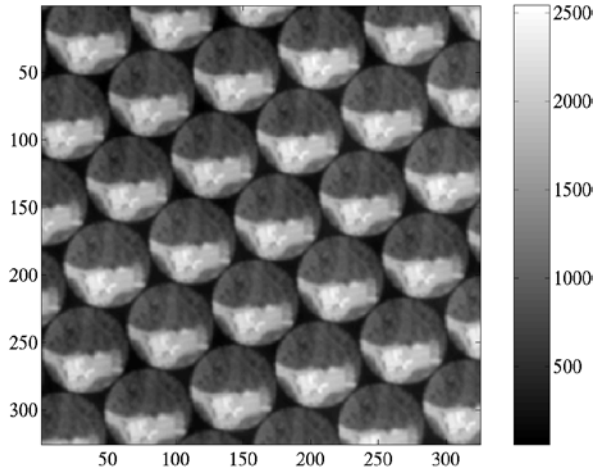

Figure 9 –An extended-scene sub-image array obtained from the convolution of the two images shown in Figures 7 and 8.

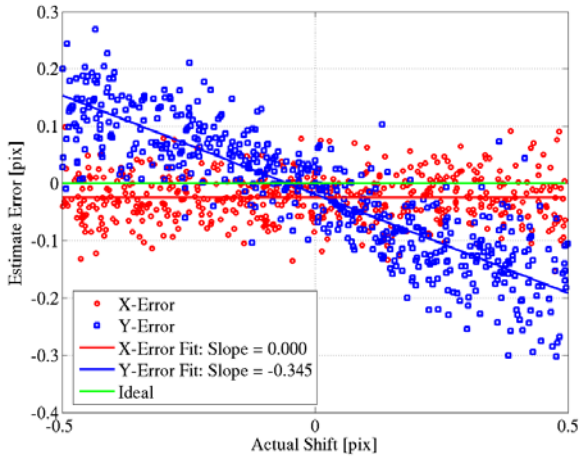

Figure 10 –Shift estimate errors of the extended-scene image shown in Figure 9.

with the spot-image in Figure 8, and generated 180 ES- SHS images with different scenes. It should be pointed out that the different cells in each sub-image array generated this way have different noise characteristics determined by the original spot-image, but the same cells, that is, the cells located at the same position, of the different sub-image arrays have the same noise characteristics. This is the ideal feature of the current sub-image arrays to study the scene-dependent shift estimate error of the APC algorithm. Therefore, no any additional noise has been introduced to the above half-real, half-synthesized extended-scene sub-image arrays.

Assume the locations of spot-images in Figure 8 are given by

$$\begin{aligned} \vec{x}_{act} &= \vec{X} + \Delta\vec{x}_{act} \\ \vec{y}_{act} &= \vec{Y} + \Delta\vec{y}_{act} \end{aligned} \tag{3}$$

were $[\vec{X}, \vec{Y}]$ are integers and $[\Delta\vec{x}_{act}, \Delta\vec{y}_{act}]$ are fractional-numbers ranging from -0.5 to 0.5 pixels. The subscript "act" means "actual". When extracting 32x32 pixels cells from the image in Figure 8, the $[\vec{X}, \vec{Y}]$ are used as their centers because no SHC sub-pixel images are available. Therefore, the reference cell has $[\Delta\vec{x}_{act}, \Delta\vec{y}_{act}] = [0, 0]$ pixels and all of the other cells in a single image have intrinsic offsets relative to the reference cell. The vector pairs of $[\Delta\vec{x}_{act}, \Delta\vec{y}_{act}]$ thus represent those intrinsic offsets or actual shifts.

Now assume the analysis of the extended-scene image in Figure 9 with the APC algorithm yields $[\Delta\vec{x}_{est}, \Delta\vec{y}_{est}]$, where the subscript "est" means "estimated". These shifts are different from the actual shifts and we refer to their differences as "shift estimate errors". That is, the shift estimate errors are defined as

$$\begin{aligned} \vec{\varepsilon}_{xuc} &= \Delta\vec{x}_{est} - \Delta\vec{x}_{act} \\ \vec{\varepsilon}_{yuc} &= \Delta\vec{y}_{est} - \Delta\vec{y}_{act} \end{aligned} \tag{4}$$

where the subscript "uc" means "un-corrected".

Figure 10 shows the shift estimate errors $[\vec{\varepsilon}_{xuc}, \vec{\varepsilon}_{yuc}]$ obtained for the image shown in Figure 9 as a function of $[\Delta\vec{x}_{act}, \Delta\vec{y}_{act}]$. The red-circle and the blue-square markers show the raw values of $[\vec{\varepsilon}_{xuc}, \vec{\varepsilon}_{yuc}]$, and the red and the blue solid-lines are their linear-fit lines. The green-line indicates where $[\vec{\varepsilon}_{xuc}, \vec{\varepsilon}_{yuc}]$ should be in an ideal case. It must be emphasized that the shift estimate errors $[\vec{\varepsilon}_{xuc}, \vec{\varepsilon}_{yuc}]$ are purely the result of changing the SHC image from spot-images in Figure 8 to an extended-scene image in Figure 9. That is why we called them "scene-content-dependent shift estimate errors". One can see that each of the two scene-content-dependent shift estimate errors, $[\vec{\varepsilon}_{xuc}, \vec{\varepsilon}_{yuc}]$, has the following three components: (1) Slope-error specified by the slope of the linear-fit line. (2) Mean error or bias. (3) Scattered-error. As we can see from Figure 10, the scattered-error is the dominant one. It is also the one built-in in the APC algorithm and we cannot do anything about it without changing the algorithm. As is well-known, the shift estimate biases give rise to a global tip-tilt of the wavefront error to be measured, and can easily be eliminated by subtracting them out from the corresponding shift estimate data. We propose to correct the shift estimate slope errors

in the following way: Assume the linear-fit lines of the $[\vec{\varepsilon}_{xo}, \vec{\varepsilon}_{yo}]$ pair are expressed by $[\vec{\varepsilon}_{xfit}(\Delta\vec{x}_{act}), \vec{\varepsilon}_{yfit}(\Delta\vec{y}_{act})]$. Then the corrected shift estimates $[\Delta\vec{x}_{cor}, \Delta\vec{y}_{cor}]$ become as

$$\begin{aligned} \Delta\vec{x}_{cor} &= \Delta\vec{x}_{est} - \vec{\varepsilon}_{xfit}(\Delta\vec{x}_{act}) \\ \Delta\vec{y}_{cor} &= \Delta\vec{y}_{est} - \vec{\varepsilon}_{yfit}(\Delta\vec{y}_{act}) \end{aligned} \tag{5}$$

where the subscript "cor" means "corrected. It should be pointed out that the above procedure also corrects the shift estimate bias errors. The after-correction shift estimate errors become as

$$\begin{aligned} \vec{\varepsilon}_{xc} &= \Delta\vec{x}_{cor} - \Delta\vec{x}_{act} \\ \vec{\varepsilon}_{yc} &= \Delta\vec{y}_{cor} - \Delta\vec{y}_{act} \end{aligned} \tag{6}$$

where the subscript "c" in $[\vec{\varepsilon}_{xc}, \vec{\varepsilon}_{yc}]$ means "corrected".

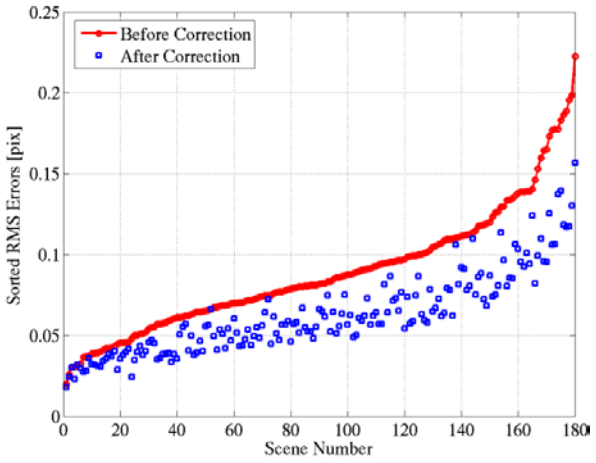

Figure 11 –Histograms of the $[\vec{\varepsilon}_{xo}, \vec{\varepsilon}_{yo}]$ slopes.

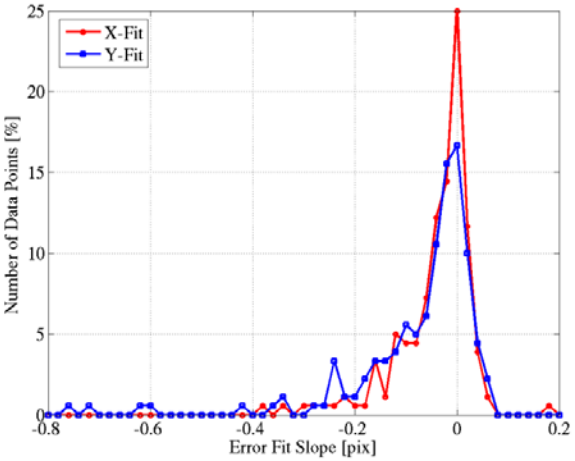

Figure 12 –Histograms of the $[\vec{\varepsilon}_{xo}, \vec{\varepsilon}_{yo}]$ slopes.

The shift estimates as well as their slopes and biases are all different for the 180 different scenes. Figure 11 shows the root-mean-square (RMS) values of the un-corrected and the corrected radial shift estimate errors, Figure 12 shows the histograms of the $[\vec{\varepsilon}_{xfit}(\Delta\vec{x}_{act}), \vec{\varepsilon}_{yfit}(\Delta\vec{y}_{act})]$ slopes, and Figure 13 shows the bias values of the $[\vec{\varepsilon}_{xo}, \vec{\varepsilon}_{yo}]$, respectively. The radial shift estimate error is defined as

$$\vec{\varepsilon}_{rs} = \sqrt{\vec{\varepsilon}_{xs}^{\,2} + \vec{\varepsilon}_{ys}^{\,2}} \tag{7}$$

with subscript s = o or c, respectively. In Figure 11, the mean values of the two sets of data are $[\overline{\sigma}_{ro}, \overline{\sigma}_{rc}]$ =[0.108, 0.076] pixels. That is, overall, the shift estimate slope error correction procedure described above reduces the RMS-error by approximately 30%. As we can see, the tails of the negative slopes of the $[\vec{\varepsilon}_{xfit}(\Delta\vec{x}_{act}), \vec{\varepsilon}_{yfit}(\Delta\vec{y}_{act})]$ are longer than the positive ones (Figure 12), meaning the estimated shifts lag the actual ones. The reason of this phenomenon has yet to be understood. The distributions of the shift estimate biases are relatively symmetric (Figure 13).

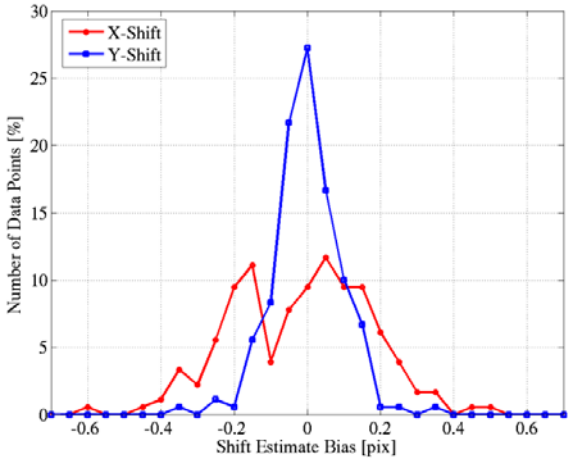

Figure 13 –Histograms of the mean values (biases) of the $[\vec{\varepsilon}_{xo}, \vec{\varepsilon}_{yo}]$.

We have also tried another five sets of extended-scene sub-images extracted from the sub-image arrays measured on our AWCT testbed. That is, we replaced the sub-image in Figure 7 with five sub-images that are part of the ES-SHS images measured with different scenes on our testbed. They had scene contents completely different from one another, and yielded $[\overline{\sigma}_{ro}, \overline{\sigma}_{rc}]$ =[0.052, 0.031], respectively. That is, the mean values of the shift estimate error standard deviations turned out to be much smaller in this case than the previous one. Also, we achieved an RMS-error reduction of ~40% this time. We expect the APC algorithm will yield results similar to that of the latter case, especially with the help of an image-content selection criterion to be implemented in the APC algorithm in the near future.

5. CONCLUSION

We presented a study about the dependence of the Adaptive Periodic-Correlation (APC) algorithm performance on the image content of extended scenes. We have divided the scene-content-dependent shift estimate errors into the following three components: Slope-error, mean-error (or bias), and scattered-error. The scattered-error component is the result of an intrinsic property of the APC algorithm itself in its current form, and dominates the whole shift estimate error. The mean-error can be eliminated completely by a simple subtraction. We have shown that the slope-error can be reduced by 30-40%, and proposed a procedure for that purpose. The material presented in this paper enables one to better understand the APC algorithm and its more robust implementation in adaptive-optics (AO) systems that conduct Shack-Hartmann-based wavefront sensing and control using either a point source or arbitrary extended scenes.

REFERENCES

[1] I. Ghozeil, "Hartmann and other screen tests,", in *Optical Shop Testing 2nd Edition*, D. Malacara, ed., pp. 367-396, Wiley, New York, 1992.

[2] Scott A. Basinger, David C. Redding, Andrew E. Lowman, Laura A. Burns, Karen Y. Liu, and David Cohen, "Performance of wavefront sensing and control algorithms on a segmented telescope testbed," Proc. SPIE Int. Soc. Eng. **4013**, 749 (2000).

[3] Lisa A. Poyneer, "Scene-based Shack-Hartmann wave-front sensing: analysis and simulation," Appl. Opt. **42**, 5807 (2003).

[4] E. Sidick, Joseph J. Green, Rhonda M. Morgan, Catherine M. Ohara, David C. Redding, "Adaptive cross-correlation algorithm for extended scene Shack-Hartmann wavefront sensing," Opt. Let. **33**, 213 (2008).

[5] E. Sidick, " Adaptive Periodic-Correlation Algorithm for Extended Scene Shack-Hartmann Wavefront Sensing," 2011 COSI Topical Meeting (OSA, Toronto, Canada, 2011), to be published

[6] F. Shi, S. Basinger, R. Diaz, H. Tang, R. Lam, E. Sidick, R. Hein, M. Rud, and M. Troy, "Advanced Wavefront Sensing & Control Testbed (AWCT)," *Proc. SPIE,* vol. **7739**, pp.7739-2W, June 2010.

[7] E. Sidick, "Dependence of adaptive cross-correlation algorithm performance on the extended scene image quality," *Proc. SPIE,* vol. 7093, pp. 70930G, August 2008.

[8] Rhonda M. Morgan, William K. Wilkie, Xiaoqi Bao, Erkin Sidick, "Actuator fault detection via electrical impedance testing," Proc. SPIE vol. 6711, pp. 67110A, August 2007.

BIOGRAPHIES

Erkin Sidick *received a B.S. in Electrical Engineering from Xinjiang University, Urumchi, Uyghur Autonomous Region, China, in 1983, an M.S. in Physics from California State University, Northridge, in 1990, and a Ph.D. in Electrical Engineering from the University of California, Davis, in 1995. He joined JPL in 2004, and is currently a Senior Member of the Technical Staff. He has worked on a variety of projects related to space telescopes, conducting optical modeling and simulations in the areas of wavefront sensing and control as well as integrated modeling. He is currently involved in the projects of Terrestial Planet Finder Coronagraph (TPF-C), Geo-Seismic Imager, as well as advanced mirror development for space telescopes.*